Turbulence and Drag in a High Reynolds Number Tidal Passage Targetted for In-Stream Tidal Power

Alex E. Hay, Justine McMillan, Richard Cheel and Douglas Schillinger
Department of Oceanography, Dalhousie University
Halifax, Nova Scotia, Canada
E-mail: alex.hay@dal.ca

***Abstract*—Results are presented from an investigation of turbulence and bottom drag carried out in Grand Passage, lower Bay of Fundy. Flow measurements were made using a broadband 600 kHz acoustic Doppler current profiler (ADCP) sampling at nearly 2 Hz, and two single-point sensors: an acoustic Doppler velocimeter (ADV) sampling at 1 Hz, and a time-of-flight velocity sensor (MAVS) sampling at 12 Hz. All instruments were bottom-mounted. The maximum depth-averaged tidal current speed was 1.6 m/s. The local bathymetry was characterized by 20 m mean water depth and ca. 0.5 m high, 8 m wavelength dunes. The ADCP was deployed to one side of the dune field; the single-point sensor platform was within the dune field.**

Due to high water clarity, the ADV correlations at moderate to high flow speeds were very low, precluding estimation of turbulence quantities. In contrast, the time-of-flight velocity data are noise free – the measurement does not require the presence of sound scatterers – and the spectra exhibit a well-defined inertial subrange. Turbulent Reynolds stress estimates from the time-of-flight sensor data yield friction velocities (u_*) and bottom drag coefficients (C_d) comparable to those determined from the ADCP profiles via the law-of-the-wall. The ratio of RMS vertical velocity variance to friction velocity in the time-of-flight data is close to 1.2, consistent with results obtained within the constant stress layer in the atmospheric boundary layer and in rough boundary laboratory experiments.

Turbulence quantities are estimated from the (de-noised) ADCP velocity spectra via the variance method, modified here for application to a sloping seabed by taking advantage of the orientation relative to the local isobaths of the orthogonal acoustic beam pair planes. Noise levels were determined from the spectra ensemble-averaged in equal mean flow speed intervals, and are very close to the manufacturer's quoted value. When the constant stress layer was sufficiently thick – i.e. during ebb tide – the RMS turbulence intensities in the lower ADCP range bins are entirely consistent with the anisotropic relationships between Cartesian RMS turbulent velocity components and u_* obtained in rough boundary wind tunnel experiments [1]; the ADCP Reynolds stresses agree with the Law-of-the-Wall shear stress estimates; and vertical profiles of Reynolds stress are very different from the linear decrease with height expected for (lower Reynolds number) straight and narrow open channel flows. During flood tide, the boundary layer was much thinner, and the lowermost ADCP bin – at 2.1 m height – was outside the constant stress layer. The pronounced asymmetries between flood and ebb (i.e. in boundary layer thickness, turbulence intensity, and C_d) are attributed to differences in upstream bathymetry.

***Index Terms*—turbulence, bottom stress, tidal power, broadband acoustic Doppler profiler, acoustic time-of-flight sensor**

I. Introduction

This paper concerns results from a field investigation of flow and turbulence in a tidal channel using bottom-mounted sensors, including an acoustic Doppler current profiler (ADCP). The use of ADCPs for turbulence measurements in the ocean was pioneered by Plueddemann [2] and Lohrmann *et al.* [3]. To estimate Reynolds stress and other second-order turbulence quantities, both of these studies implemented the so-called variance method, whereby the limitations intrinsic to the divergent ADCP beam geometry in turbulent flow are overcome by assuming that time-averaged second-order products of the velocity fluctuations are statistically homogeneous in the horizontal: i.e. on the scale of the beam separation. The variance method was subsequently implemented by Gargett [4], by Stacey *et al.* [5], by Lu *et al.* [6], and by Rippeth *et al.* [7]. Factors contributing to errors in the method are discussed in Lu and Lueck [8] and Williams and Simpson [9]. Very recently, Vermeulen *et al.* [10] have used two ADCPs in a master-slave configuration to determine each of the terms in the Reynolds stress tensor.

With the growing interest in the potential of electrical energy generation via in-stream turbines, Doppler profiling systems are being used extensively for site characterization and resource assessment [11]. A design question for turbine developers is the turbulence intensity in these high Reynolds number flows at mid-depth, i.e. at "hub height", and concerns exist in the community as to the accuracy/reliability of estimates made using ADCPs in part because of the possible effects of flow inhomogeneity [12].

The results to be presented were obtained in September 2012 in Grand Passage, located in the lower Bay of Fundy, Nova Scotia. Grand Passage has been selected as a site for in-stream tidal power development under the Nova Scotia community feed-in tariff program. Linked to a more comprehensive resource assessment project, the September 2012 experiment was a pilot study of turbulence in the Passage. Our primary goal was to determine whether bottom-mounted measurements of turbulence with a point sensor and a broadband ADCP would be comparable, both to each other and to the known properties of turbulence in comparable geophysical flows: e.g. the atmospheric boundary layer [1] [13].

The order of presentation follows the storyline of the experiment and subsequent analysis. From the outset, identifying a suitable point sensor was non-trivial because of the high water clarity in the Passage. In addition, the measures taken to avoid contamination of the point sensor measurements by frame-generated flow disturbances led to these measurements

being available only during the flood tide. Consequently, our initial focus when comparing the point sensor and ADCP measurements was on the flood tide. The results during flood indicated that, while the MAVS-derived estimates of turbulence quantities – i.e. the dependence of RMS vertical turbulence intensity on friction velocity – were in agreement with the atmospheric boundary layer measurements, the ADCP-derived estimates were significantly lower. This rather worrisome result remained even after extensive cross-checks and re-analysis of the data. Hints of a possible explanation were indicated by the RMS vertical turbulence intensity during ebb tide and, as will be shown, resolution of the apparent difficulty is connected to the very large difference in the boundary layer thickness between ebb and flood. In addition, en route to achieving resolution we make use of the alignment of the ADCP transducer axes relative to the local bathymetry to implement the variance method in a specialized form suited to elucidating the vertical structure of Reynolds stress and turbulent kinetic energy dissipation above a sloping bed.

II. Study Site and Instrumentation

The instrument pod locations are shown relative to the large scale Grand Passage bathymetry in Fig. 1, and relative to the dune field characterizing the local bathymetry in Fig. 2. The dune height and wavelength are ca. 0.5 m and 8 m respectively (Fig. 3). The ADCP pod was deployed nearby but outside the dune field (Fig. 2).

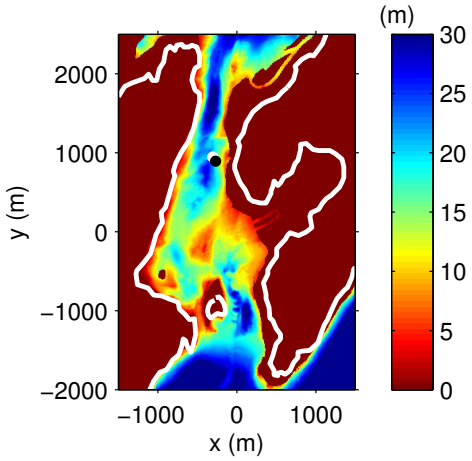

Fig. 1. Grand Passage bathymetry, from multi-beam sonar surveys. The turbulence and ADCP pod locations are indicated by the solid white and black circles, respectively. The xy origin corresponds to the mean latitude and longitude within the domain: $44.2662°$N and $-66.3346°$W respectively.

A. Turbulence Pod

The turbulence pod (Fig. 4) was constructed from mainly non-magnetic materials: solid fibreglass rod, a fibreglass grating base, and three 100 pound lead feet. Also visible are the PVC cannisters for the float-line acoustic release system, and the flat-lying PVC tube for the SubSeaSonics burn-wire acoustic release. The vertical legs were schedule 40 steel

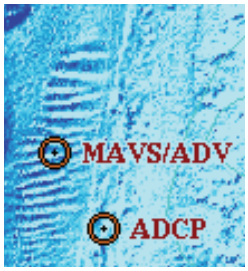

Fig. 2. Shaded multi-beam image of the dune field, with the locations of the turbulence pod (ADV/MAVS) and ADCP pod (ADCP) indicated.

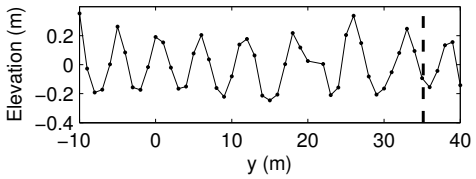

Fig. 3. Detrended bed elevation profile along a South-to-North line through the turbulence pod location, illustrating the 0.5 m high, 8 m wavelength dunes. The dashed line indicates the y location of the pod.

pipe, for added stiffness. Two high resolution single point velocity sensors – an acoustic Doppler velocimeter (ADV, Nortek Vector) and a time-of-flight velocity sensor (MAVS, Nobska Instruments) – were mounted on cantilever supports to minimize the influence of the pod on the flow measurements. Fig. 5 is a sketch of the pod in plan view, showing the orientation of the frame relative to the flow direction during flood tide. The cantilevered sensors were directed into the flow during flood, but were in the frame wake during ebb. Hence, estimates of turbulence quantities from this pod are reported for flood tide only.

The ADV velocity data were noisy. The high noise levels were associated with low correlations, and these low correlations occurred during periods of high flow, as indicated in Fig. 6. Correlations decreased with increasing flow speed despite somewhat higher backscatter amplitudes: for flow speeds exceeding 0.5 m/s the 2-min, 3-beam average correlations fell below 60%, and the 2-min, 3-beam average amplitude rose only slightly and did not exceed values of 110 arb. units (not shown). We had encountered low correlations previously in consecutive 1-day deployments in Grand Passage with the ADV mounted even closer to the bed on a frame similar to the ADCP pod. Progressively decreasing the sampling rate from 16 Hz to 1 Hz led to acceptable spikiness in the velocity record. We concluded that the scatterer concentrations in Grand Passage are too low to measure turbulence reliably with the Vector ADV, even near the bed. (Bottom photographs indicate that the dunes in Fig. 2 are composed of shell hash and gravel, with very little fine sediment.) Thus, for the present experiment the ADV was set to sample at 1 Hz for the purpose of measuring the mean flow. The other user-

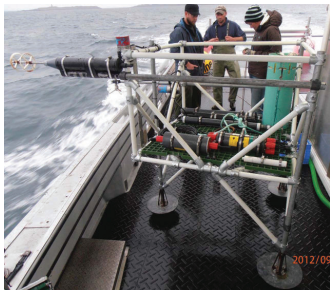

a Overall view. Note the single float-line cannister (turquoise), and the three 100 lb ballast feet, only one of which is on the velocity sensor side of the frame.

b The velocity sensors: the MAVS (upper left, foreground), and the Vector ADV (middle, background), both cantilevered away from the main body of the pod.

Fig. 4. Turbulence pod

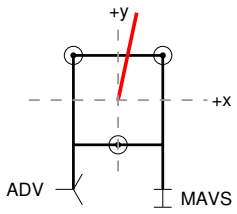

Fig. 5. Plan view sketch of the turbulence pod, roughly to scale except for the symbols indicating the ADV and MAVS. Open circles are the three 100 pound feet. The red line indicates the mean flow direction during flood tide, 12° clockwise relative to the pod y-axis. The direction of the depth-averaged flood current, determined from the ADCP data, was 7.6° True. Thus, the turbulence pod y-axis was directed ca. 5° counterclockwise from True North, and approximately normal to the dune crests (Figure 2).

settable parameters for the ADV were: maximum transmit power, maximum transmit pulse length (8 mm), and maximum sampling volume (22 mm).

Because of the high water clarity, a Nobska MAVS (Modular Acoustic Velocity Sensor) was used for the high-frequency flow measurements. The MAVS measurement is based on acoustic travel time along multiple fixed paths [14], and so does not require the presence of scatterers. The acoustic transducer elements are embedded in the two white plastic rings visible in Fig. 4. These rings are mounted on a central shaft which, for flow directed transverse to the shaft axis, leads to vortex shedding and contamination of the turbulence

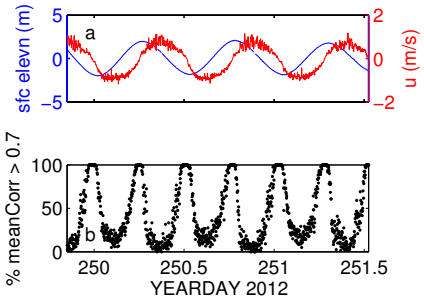

Fig. 6. ADV data: (a) surface elevation and u velocity (positive southward); (b) % 3-beam mean correlation > 0.7.

signal [15]. For flow directed parallel to the shaft axis, this contamination is much reduced: i.e. the orientation of the MAVS during flood tide (Fig. 5). The MAVS was mounted 1.45 m above bottom, and sampled at 12.35 Hz for 16.2 minutes every half hour. For estimating turbulence quantities, a coordinate system aligned with the record-mean flow direction was implemented. The resulting record-mean values of flow speed, vX, and azimuth angle, θ and tilt from the horizontal, $\phi - 90$, are plotted in Fig. 7. (During ebb tide, vX corresponds nominally to the ADCP and MAVS u component, but of course is positive for both flood and ebb so is not the same.) The red points indicate flood, the blue points ebb. The values of vX during ebb are much less than flood, apparently an effect of the wake from the MAVS pressure case, given the comparison to the ADV speeds (Fig. 7c). The values of $\phi - 90$ during flood are ca. 10°, consistent with the 10 degree tilt of the frame (registered by the ADV pitch and roll sensor). Also plotted in Fig. 7 are the values of the friction velocity, u_*, computed from the MAVS turbulence measurements, and discussed in §III-A.

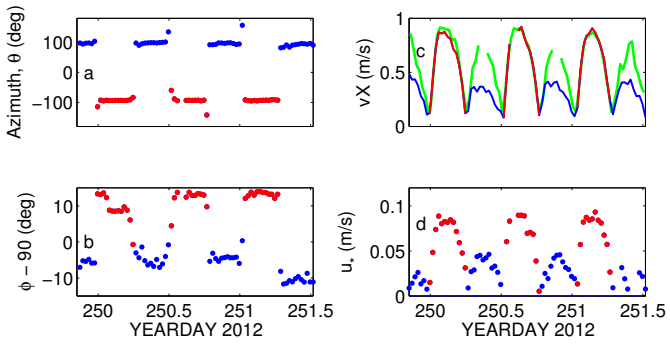

Fig. 7. MAVS. a. and b. Flow directions in instrument co-ordinates: azimuth, θ and polar, ϕ, respectively. c. Flow speed, vX, after rotation into the direction of the mean flow (i.e. the average over the 16 min record). Values during flood are indicated in red. Note the reduced speeds during ebb, attributed here to the wake of the MAVS pressure case, given the mean ADV speed time series, indicated by the green line (see also Figures 4 and 5).

As one indicator of MAVS data quality, the wavenumber spectrum of vX is plotted in Fig. 8. This spectrum is the ensemble average of all spectra during the flood tide with $vX = 0.9 \pm 0.1$ m/s. Included in the plot are two $k^{-5/3}$ fits,

one accounting for aliasing and one not. An inertial subrange is clearly present, and the fit including aliasing indicates that the inertial subrange extended beyond the Nyquist wavenumber, 43 m^{-1}. As the corresponding eddy scale is 0.15 m, and the distance between the MAVS transducer rings is 0.07 m, aliasing is just at the edge of being a physically reasonable explanation for the departure from -5/3 at high wavenumbers in Fig. 8, the goodness of fit notwithstanding.

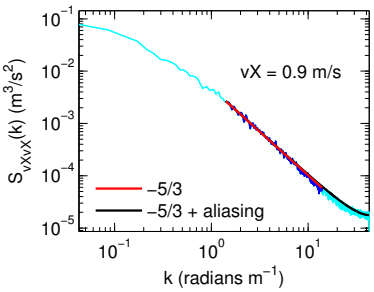

Fig. 8. MAVS. The radian wavenumber spectrum of vX, showing the fit to the -5/3 inertial subrange both with and without allowing for aliasing. The cyan (light blue) color indicates the entire spectrum; dark blue the region used for the fit. $U = 0.9$ m/s.

B. ADCP Pod

The low-profile ADCP pod (Fig. 9) was also constructed from non-magnetic materials: solid fibreglass rod, fibreglass grating, the stainless steel cage around the ADCP, and three 100-pound lead feet. Dual release systems were used in this deployment, for redundancy. The ADCP was a 600 kHz RD Instruments Workhorse, sampling at 1.83 Hz (2-ping ensembles) in 0.5 m range bins. The first bin was at 2.1 m height above bottom.

Fig. 9. ADCP pod, with dual float line cannisters.

Important in the context of the results to be presented, the bottom contours in the vicinity of the ADCP pod were nearly linear on 10 m horizontal scales, and aligned North-South (Fig. 10a). The bottom slope at this site was 5.5°.

The orientation of the ADCP relative to the True North and the ebb/flood flow directions is sketched in Fig. 10b. As will become apparent later, it is important to note that the axis from transducer 2 to transducer 1 is nearly aligned with True North and therefore parallel to the bottom contours (cf. Fig. 10a), and thus the transducer 3 to 4 axis is directed nearly up-slope. These directions are consistent with the signs and magnitudes of the pitch and roll, plotted in Fig. 11: i.e. the pitch (rotation

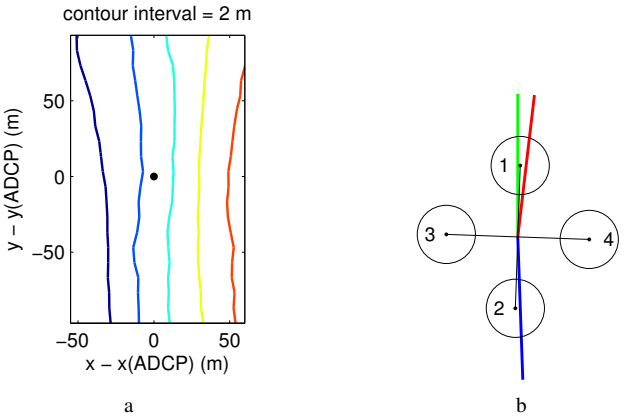

Fig. 10. (a) Bottom contours in the vicinity of the ADCP pod (black dot). Warmer contours are shallower. The contour interval is 2 m, the deepest (dark blue) is 22 m; the shallowest (red) 14 m. (b) ADCP orientation. The solid green and red lines indicate the directions of true North and the flood tide, the latter as in Fig. 5. The blue line is the ebb tide direction. The numbers indicate the different transducers in the Janus configuration, following the convention used by RD Instruments.

about the 1-2 axis) is negative and ca. -8°, consistent with the -5.5° bottom slope, while the roll (rotation about the 3-4 axis) is small, $< 0.5°$, consistent with this axis being directed parallel to the bottom contours. Note also that after an adjustment during the first hour, the values of heading, pitch and roll are all very steady, indicating that the ADCP pod orientation remained stable over the 3 day deployment.

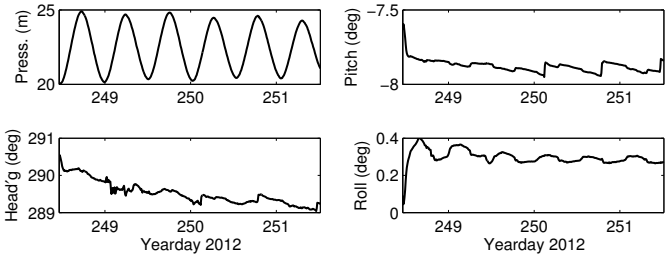

Fig. 11. Time series of ADCP attitude parameters: (a) pressure; (b) heading; (c) pitch and (d) roll.

III. Results

A. MAVS

The horizontal and vertical velocity spectra from the MAVS, ensemble-averaged in 0.2 m/s wide vX speed bins, are plotted in Fig. 12. For notational simplicity, vX and vZ are denoted u and w from here forward. In Fig. 12, the frequency at which the spectra depart from the -5/3 behaviour at high frequencies increases with mean flow speed, which would not occur if this departure from -5/3 were due to aliasing alone. Instead, a noise floor is indicated, which appears to increase with flow speed. It is only at the highest flow speeds that the spectral densities are far enough above the noise that aliasing accounts for the departure from -5/3 (i.e. Fig. 8).

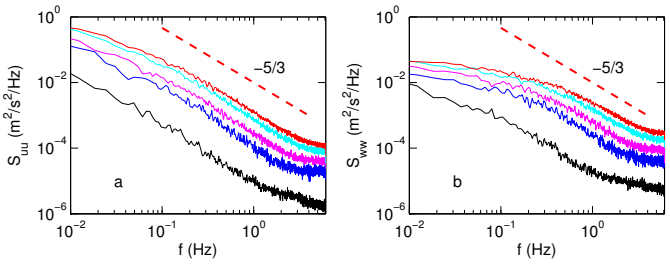

Fig. 12. MAVS velocity spectra during flood tide, averaged in 0.2 m/s mean speed intervals centred on 0.1, 0.3, 0.5, 0.7 and 0.9 m/s (black, blue, magenta, cyan,red).

The fluctuations u' and w' were obtained by removing the mean and trend from each 16 minute record of u and w, yielding estimates of the Reynolds stress, $-\langle u'w'\rangle = u_*^2$, where u_* is the friction velocity. In Fig. 13a, the square-root of the variance of w', σ_w, is plotted versus u_* and shown to compare favorably with

$$\sigma_w = 1.2u_*. \tag{1}$$

The above relation is based on measurements within the near-bed constant stress layer both in laboratory flow over rough boundaries ([1], [16]) and in the atmospheric boundary layer [13]. For open channel flows, [17] (see also [5]) suggest a slightly different relationship, $\sigma_w = 1.25u_*$. The above-mentioned noise floor in the MAVS data would contribute to σ_w but not to u_*, provided the noise in u' and w' are uncorrelated. Taking 10^{-4} m^2/s^2 as the S_{ww} noise level at higher flow speeds (Fig. 12b), and assuming white noise, the contribution from noise to σ_w would be ca. 0.01 m/s: i.e. only a 10% contribution to the values of σ_w at high flow speeds.

The agreement with previous boundary layer turbulence results indicates that the turbulence measurements made with the MAVS in this experiment are accurate, and lays the basis for the assessment in the remainder of the paper of turbulence quantities estimated from the ADCP data. Part of that comparison includes the bottom drag coefficient, C_d. The value of C_{d1m} referenced to the mean flow at 1 m height, U_{1m}, is 12×10^{-3} (Fig. 13a). U_{1m} was determined from the MAVS data assuming constant stress (i.e. u_* independent of z).

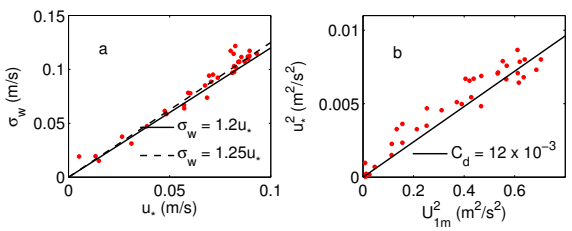

Fig. 13. MAVS data, flood tide. (a) RMS vertical velocity σ_w vs. u_* (determined from the Reynolds stress). The solid line is Eq. 1. (b) Reynolds stress vs squared mean velocity at 1 m height. The solid line is the least squares best linear fit, yielding the indicated value of C_{d1m}.

B. ADCP

Representative beam-coordinate velocity spectra computed from the ADCP data are shown in Fig. 14. The spectra are designated S_{22}: i.e. the spectral density of the beam 2 radial velocity. The values shown are for 6.1 m height, and have been ensemble-averaged both over 5 adjacent bins (2.5 m) in the vertical, and within the 0.4 m/s speed bins. The measure of speed used was the 5-bin average at this height. A noise floor is clearly evident in the frequency spectra (Fig. 14a), with a value of 2.6×10^{-3} m^2/s^2/Hz, common to all four speed intervals except possibly the highest which exhibits a hint of aliasing. Though not shown here, this same noise level was observed in all 4 beams and for all range bins and, given the 0.92 Hz Nyquist frequency, corresponds to a velocity standard deviation, $\sigma_V = 0.049$ m/s. For comparison, the expected accuracy given by the manufacturer's setup software for the settings used here (0.5 m bins, 2-ping ensembles) is 0.096 m/s in the *horizontal* velocity: i.e. σ_u. Conversion to the corresponding error in the along-beam velocity requires multiplying σ_u by $\sqrt{2}\sin\theta$, θ being the 20° beam inclination angle, giving $\sigma_V = 0.046$ m/s, close to the value indicated by the observed noise levels in the beam velocity spectra.

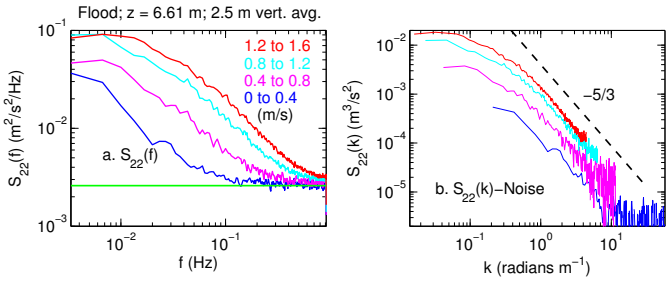

Fig. 14. ADCP beam 2 velocity spectra, averaged over 5 range bins centred on at 6.6 m height, during flood tide. The spectra have been ensemble-averaged in 0.4 m/s speed bins, as indicated in the legend: (a) frequency spectra, including the noise floor (green); (b) wavenumber spectra, with the noise floor subtracted off.

The spectra in Fig. 14 indicate a well-defined inertial subrange, which justifies examining the variation of σ_w with u_* in the ADCP data in comparison to Eq. 1 and the MAVS data (i.e. Fig. 13). Values of σ_w were determined by integrating the spectrum of the vertical velocity in each bin, after subtracting a noise floor, in 10-minute intervals. The vertical velocity noise floor determined from the spectra was 0.0294 m^2/s^2/Hz. The resulting estimates of σ_w for the range bin nearest the bed during flood tide are plotted in Fig. 15a versus u_* determined from the law-of-the-wall.

$$\kappa U(z) = u_* \ln[z/z_0] \tag{2}$$

with the von Karman constant κ set to 0.4, using 10-min mean speeds, and non-linear least squares fit to the lowermost 8 bins of the speed profile.

The σ_w values in Fig. 15a fall well below $1.2u_*$, by a factor of 4. The results in adjacent range bins farther from the bed are very similar (not shown). The factor of 4 underestimate of σ_w

in the present results is a concern, as it would indicate that estimates of turbulence kinetic energy using high-resolution ADCP data might be underestimated by a factor of 16. Furthermore, the underestimate is in the vertical velocity component, which is the most accurate velocity component measured in the 4-beam Janus transducer geometry. Finally, the underestimate is especially a concern in the present context given the very good agreement between the MAVS data (Fig. 13a) and Eq. 1 at a similar height above bottom (1.45 vs. 2.1 m). An explanation is required.

In seeking an explanation for the anomalous result in Fig. 15a, it is useful to check the values of u_*, as one possibility is that σ_w is not small and rather that the u_* values are unrealistically high. The associated values of shear stress, u_*^2, are plotted versus U_{1m}^2 in Fig. 15b, where again U_{1m} was determined assuming a constant stress layer, yielding values for C_{d1m}. During flood tide, $C_{d1m} = 9.5 \times 10^{-3}$, which is comparable to but 20% lower than the MAVS value on flood. The lower value is attributable to differences in bottom roughness at the two sites: i.e. the absence of dunes at the ADCP pod location (Fig. 2). We conclude that the u_* values are not grossly (i.e. by a factor of 4) overestimated.

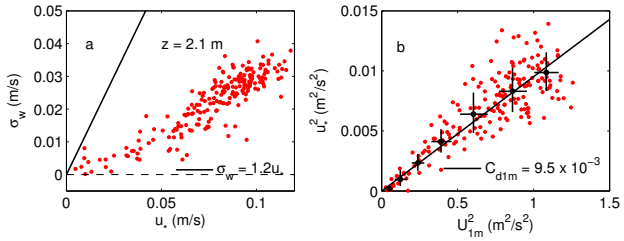

Fig. 15. ADCP data, flood tide. (a) RMS vertical velocity σ_w at 2.1 m height vs. u_* determined from the law-of-the-wall. The solid line is Eq. 1. (b) Stress vs. squared mean velocity at 1 m height. The black points are the means within 0.2 m/s speed intervals, with error bars representing ± 1 standard deviation. The solid black line indicates the best fit through the origin, yielding the indicated value of C_{d1m}. The red points in (a) and (b) indicate values based on 10-minute average.

A hint at where the explanation may lie is provided by Fig. 16, in which are plotted the same results as those in Fig. 15, except for ebb tide. Note that these values of σ_w, while still less than $1.2u_*$ are comparable to those in Fig. 15a, but distributed over a reduced range of u_* values. The best-fit value of C_{d1m} during ebb is also less than that during flood, by about 30%.

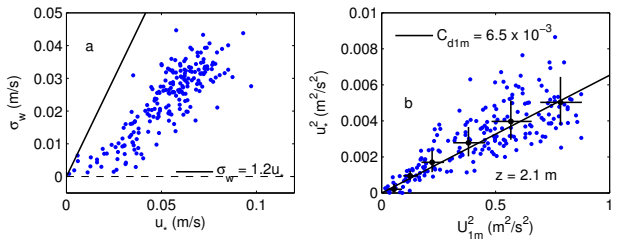

Fig. 16. As in Fig. 15, except for ebb tide.

The differences between flood and ebb conditions are pursued via Fig. 17, in which are plotted the vertical profiles of mean speed, ensemble-averaged in 0.2 m/s speed bins based on the speed at 5 m height. This height was chosen as being representative of the flow in the outer part of the boundary layer, but below the $z > 10$ m zone of negative shear present during flood tide at higher flow speeds especially. The vertical extent of the logarithmic profile is strikingly different between flood and ebb, sometimes throughout the water column during ebb, but confined to the first 4 range bins (i.e. below 5 m height) during flood. It is known from windtunnel measurements of turbulence over rough beds that, for heights above the near-bed constant stress layer, Eq. 1 does not apply and σ_w decreases with height instead. The data in Fig. 17 suggest that the relationship between σ_w and u_* should be examined during ebb, the hypothesis being that the much thicker boundary layer would ensure that the constant stress layer extended at least as high as the first range bin.

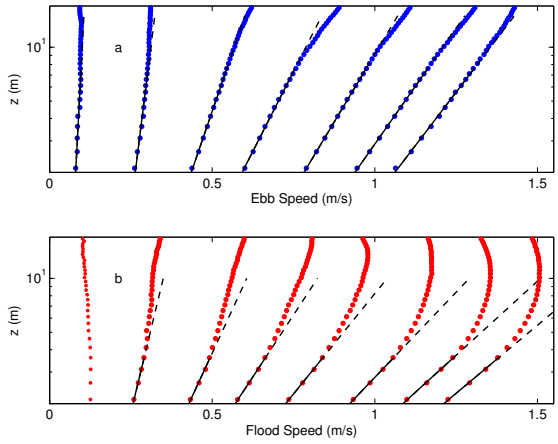

Fig. 17. Vertical profiles of mean speed, based on 10 min average ADCP East-North velocities, ensemble-averaged within 0.2 m/s speed intervals based on the 10 min average speed at 5 m height. The solid black lines are the law-of-the-wall fits, the dashed black lines their extension to 10 m height. For the ebb profiles 12 bins were used for the fits; for flood, only 4. Note the much thicker boundary layer during ebb.

To test the above hypothesis it is appropriate to work with beam coordinate velocities, partly because bottom slope effects on the Cartesian velocity component are not involved, and partly because the bottom slope affects only beams 3 and 4 which are transverse to the flow direction (Fig. 10b). Let uvw represent the xyz Cartesian velocity components in a right-handed coordinate system with z normal to the bottom and positive upward. Note that z is not vertical: i.e. not antiparallel to local gravity. Let u be the flow parallel to the bottom contours, and positive southward. Then, with the beam velocities positive toward their respective transducers, and referring to Fig. 10b, during ebb tide the beam velocities $V1$ and $V2$ for transducers 1 and 2 are related to u and w only and given by

$$V1 = u \sin\theta - w \cos\theta \tag{3}$$

and

$$V2 = -u\sin\theta - w\cos\theta, \tag{4}$$

where w is positive upward and θ is the beam tilt angle relative to z for the Workhorse ADCP. Thus, the turbulent fluctuations are given by $V' = \pm u'\sin\theta + w'\cos\theta$, and the $V1$ and $V2$ variances become

$$\sigma_{V1}^2 = \sigma_u^2\sin^2\theta + \sigma_w^2\cos^2\theta - \langle u'w'\rangle\sin 2\theta \tag{5}$$

$$\sigma_{V2}^2 = \sigma_u^2\sin^2\theta + \sigma_w^2\cos^2\theta + \langle u'w'\rangle\sin 2\theta. \tag{6}$$

Now, noting that $u_*^2 = -\langle u'w'\rangle$ and invoking the relationships indicated by the wind tunnel measurements [16] [1] between the Cartesian velocity second-order moments: i.e. $\sigma_u \sim 2u_*$ and $\sigma_w \sim 1.2u_*$ (i.e. Eq. 1), and setting $\theta = 20°$, we obtain $\sigma_V \sim u_*\left[0.47 + 1.27 \pm 0.64\right]^{1/2}$ and thus

$$\sigma_{V1} \sim 1.54u_* \tag{7}$$

$$\sigma_{V2} \sim 1.05u_*. \tag{8}$$

Similarly but in the direction transverse to the flow, with $\sigma_v \sim 1.4u_*$ [1], [16], $\sigma_w \sim 1.2u_*$ again, and $\overline{v'w'} = 0$, $\sigma_V \sim u_*\left[0.23 + 1.27\right]^{1/2}$ yielding

$$\sigma_{V3}, \sigma_{V4} \sim 1.22u_*. \tag{9}$$

The relationships in Eqs. 7 through 9 are compared to the data in Fig. 18, where the u_* values are from the Law-of-the-Wall. The σ_V values were determined by integrating the S_{VV} spectra: i.e. as was done for the flood tide results in Fig. 15a. Note in this respect that same 0.0026 m^2/s^2/Hz noise level evident in Fig. 14 for *flood* tide, and *higher in the water column* (i.e. 6.6 m vs. 2.1 m) was subtracted from the S_{VV} spectra prior to integrating to obtain the σ_V estimates in Fig. 18.

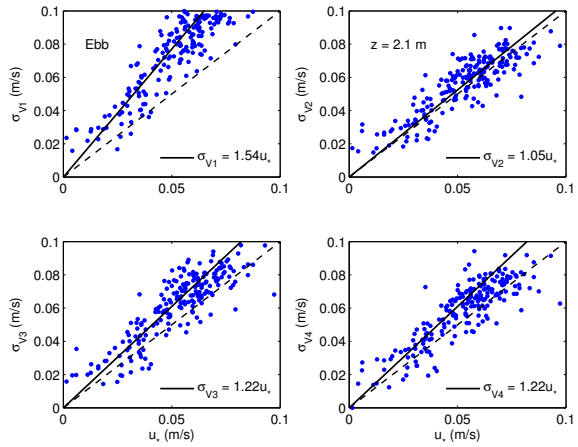

Fig. 18. ADCP RMS beam velocities in the first range bin, plotted vs. u_* (from the Law-of-the-Wall) during ebb tide, compared to the empirical σ_V vs. u_* relationships in Eqs. 7, 8 and 9 (solid black lines). The dashed 1:1 lines are included for reference.

The agreement exhibited in Fig. 18 between the ADCP data and Eqs. 7 through 9 is very good. This result indicates that, *during ebb tide*, when the logarithmic boundary layer essentially spanned the entire water column (Fig. 17a), the ADCP bin nearest the bed was in the constant stress layer. In contrast, the equivalent results for *flood tide* (Fig. 19) indicate that the observed second moments are less than the predicted values for all four beams. It follows that our hypothesis regarding the observed underestimate of σ_w in Fig. 16a is correct: the much thinner boundary layer during flood tide results in the first ADCP bin being outside the constant stress layer.

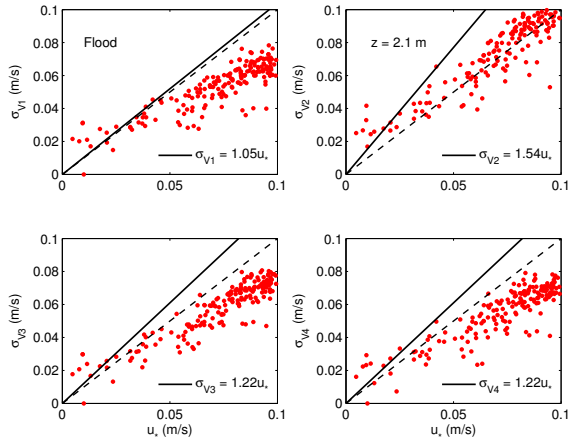

Fig. 19. As in Fig. 18, but for flood tide. The relations for beams 1 and 2 are reversed due to the change in sign of u.

C. ADCP Measurements of Reynolds Stress

A further check on the validity of the ADCP estimates of turbulence quantities in the context of the present data set is to compare estimates of the Reynolds stress $-\langle u'w'\rangle$ to Law-of-the-Wall values of u_*^2. From Eqs. 5 and 6, the Reynolds stress is

$$-\langle u'w'\rangle = [\sigma_{V1}^2 - \sigma_{V2}^2]/[2\sin 2\theta]. \tag{10}$$

Ebb tide Reynolds stresses at 2.1 and 4.1 m height are plotted against the Law-of-the-Wall values of u_*^2 in Fig. 20. The $-\langle v'w'\rangle$ values of transverse stress are near zero on average, as expected. The absolute value of the longitudinal Reynolds stress, $-\langle u'w'\rangle$, is comparable (on average) to the log-law estimates. These data also indicate a tendency for $|\langle u'w'\rangle|$ to be lower than (log-law) u_*^2 at high values of the stress.

The comparable relationships between Reynolds stress and (log-law) u_*^2 at the two different heights in Fig. 20 suggest a constant stress layer. Profiles of Reynolds stress are plotted in Fig. 21, normalized by the square of the values of u_* obtained via the Law-of-the-Wall. The ebb tide and flood tide profiles are very different.

During flood tide the $-\langle u'w'\rangle/u_*^2$ profiles collapse nicely, and above 3 m height fall off linearly to near zero values as the surface is approached (Fig. 21b). This linear decrease with height is similar to the result obtained by [5] in a straight, narrow, 10 m deep channel. A linearly decreasing stress profile is expected for steady uniform open channel turbulent flow

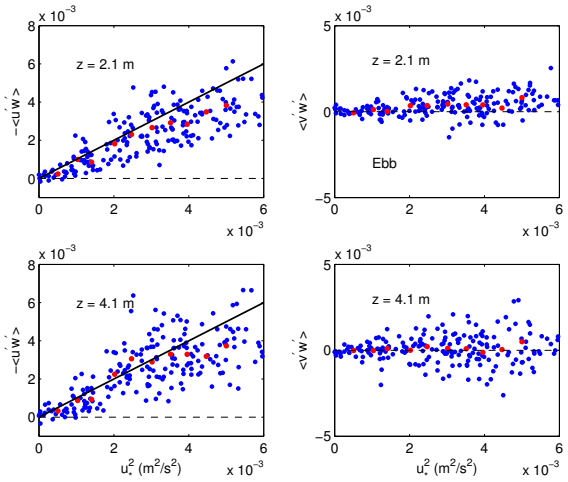

Fig. 20. ADCP Reynolds stresses vs. u_*^2 (u_* from the Law-of-the-Wall) during ebb tide at 2.1 and 4.1 m height. Red points indicate averages in 0.005 m^2/s^2 intervals of u_*^2. Solid black line is the 1:1 line.

outside the viscous/roughness sublayer [17]. However, the ratio $|\langle u'w'\rangle|/u_*^2$ should tend linearly to unity as the bed is approached, but does not here. Instead, below 3 m height the Reynolds stress increases toward the bed more rapidly, consistent with the thin near-bed log layer in the flood tide speed profiles (Fig. 17b). Extrapolating the linear region above 3 m height to the bed in Fig. 21b would yield a value less than unity for the ratio of the two stress estimators: i.e. ca. 0.4. Note that decreasing the flood tide log-law stress estimates by a factor of 0.4 would yield $C_{d1m} = 3.8 \times 10^{-3}$ instead of 9.5×10^{-3} (cf. Fig. 15b): i.e. arguably somewhat closer to the 6.5×10^{-3} ebb tide value (Fig. 16b).

In contrast, during ebb the overall tendency among the $-\langle u'w'\rangle/u_*^2$ profiles is to be roughly constant below 10 m height before falling off toward zero as the surface is approached. A linear increase toward the bed is not observed. Also, on average, the values of $|\langle u'w'\rangle|/u_*$ below 10 m do approach unity. The ebb tide profiles do not collapse well however, possibly indicating a need for longer time series to obtain better statistics: i.e. more realization to permit the use of narrower speed bins, for example. That this is a reasonable suggestion is indicated by the fact that variations among the profiles in Fig. 21a do not exhibit any obvious dependence on speed.

D. Dissipation Estimates

For locally isotropic turbulence, the relationships between the spectral densities $S_{uu}(k)$ and $S_{ww}(k)$ in the inertial subrange and the rate of dissipation of turbulent kinetic energy ϵ are given by

$$S_{uu}(k) = C_1 \epsilon^{2/3} k^{-5/3}; \quad S_{ww}(k) = C_1' \epsilon^{2/3} k^{-5/3} \qquad (11)$$

where the Kolmogorov constants C_1 and C_1' take the values 0.5 and 0.65 [18]. Replacing the variances in Eqs. 5 and 6 with the respective spectral densities it follows from Eq. 11

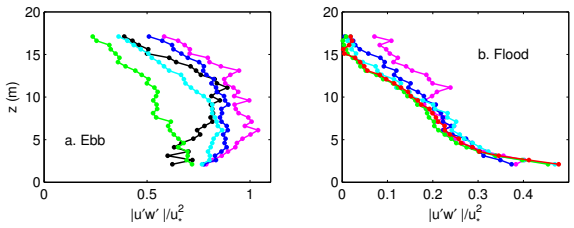

Fig. 21. ADCP Reynolds stress profiles normalized by u_*^2 (u_* from the Law-of-the-Wall) during: (a) ebb tide; and (b) flood. The profiles are ensemble averages within 0.2 m/s wide mean speed intervals based on the speed at 5 m height: i.e. black, magenta, blue, cyan, green, and red in ascending order of mean speed.

that, in the inertial subrange,

$$S_{11}(k) + S_{22}(k) = 2\epsilon^{2/3} \left[C_1 \sin^2\theta + C_1' \cos^2\theta\right] k^{-5/3} , \qquad (12)$$

or

$$\epsilon = 0.70 \left[S_{11}(k) + S_{22}(k)\right]^{3/2} k^{5/2} . \qquad (13)$$

Estimates of ϵ were obtained from the denoised spectral densities S_{11} and S_{22} averaging over the 2 to 4 radian/m range of wavenumbers after first multiplying by $k^{5/3}$. The resulting values at 2.1 m height are ca. 3×10^{-4} W/kg at 1 m/s mean speed for both flood and ebb (Fig. 22). In comparison, dissipation estimates from the MAVS spectra based on the best-fit to an aliased -5/3 spectrum, as in Fig. 8, are ca. 1×10^{-3} W/kg at 0.9 m/s for both the S_{uu} and S_{ww} spectra (flood tide only, of course). Recalling that the MAVS was located closer to the bed (1.45 m vs. 2.1 height for the first ADCP bin) and in the dune field, it seems not unreasonable that the MAVS values of ϵ would be a factor of 3 or so higher than the ADCP estimates.

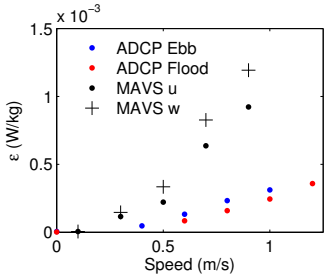

Fig. 22. Dissipation estimates. The ADCP estimates are from the first bin, at 2.1 m height.

IV. Discussion

A. Ebb/Flood Asymmetry

The preceeding results indicate pronounced differences in the vertical structure of flow and turbulence quantities between ebb and flood tide, including the bottom drag coefficient. The question is why this should be the case. The water column is unstratified, a result of the vigorous tidal mixing and absence of freshwater runoff in the area. The bottom at the ADCP site is locally uniform on 10 m and larger horizontal scales,

with straight and parallel contours. The answer must therefore almost certainly have to do with differences in upstream bathymetry. To the north of the ADCP location, i.e. in the upstream direction during ebb, a prominent ridge extends into the channel from the eastern side (Fig. 1). This ridge and the associated shoal extending from the shoreline are sources of eddies and macro-scale turbulence which are then advected past the ADCP site. Evidence for increased eddy energy during ebb is presented in Fig. 23: the variance of the high-frequency motion (periods shorter than 20 min) is greater during ebb than flood. We suggest that the vertical mixing associated with these eddies is responsible for the much thicker – essentially water column filling – boundary layer during ebb.

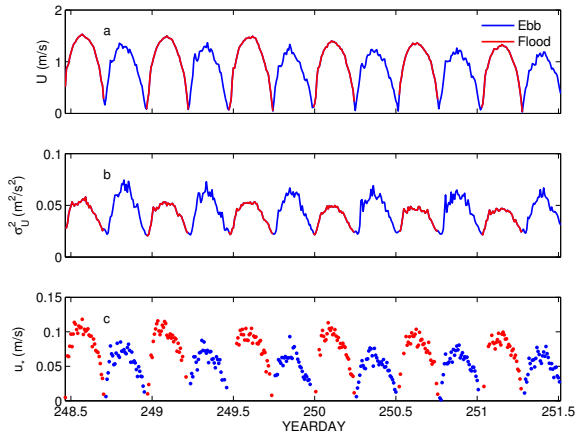

Fig. 23. Time series of vertical and 10-minute time averages of: (a) mean speed (b) high-frequency (20 min cutoff period) velocity variance; and (c) log law u_*.

During flood tide, the vertical profiles of both Reynolds stress (Fig. 21b) and speed (Fig. 17b) indicate the presence of a thin near-bed boundary layer below a second, thicker shear layer: i.e. a layer of linearly decreasing Reynolds stress and quasi-logarithmic dependence of speed on height. Within this thin nearbed layer, the higher stresses compared to the overlying layer of weaker shear and lower Reynolds stress result in the higher values of the bottom drag coefficient on flood compared to ebb tide.

Returning to Fig. 23, note that the depth-averaged mean speed is higher during flood than during ebb. Thus we are led, finally, to the following counter-intuitive result: the *constant stress layer is much thinner during flood tide* than during ebb, too thin to be observed in the ADCP profiles in fact, despite the fact that *the mean flow speed is higher during flood* than during ebb. The implication is that, during flood, the constant stress layer does not have sufficient time to grow to a height of 2 m, whereas during ebb the eddies shed from the upstream ridge promote more rapid boundary layer growth, analogous (in the wide sense) to tripping a laminar boundary layer on a flat plate with a single roughness element.

B. Implications for In-Stream Tidal Energy

The very different conditions between ebb and flood identified here (i.e. in the vertical structure of the mean flow, in the high-frequency velocity variance, and in the turbulent shear stress) would clearly have implications for tidal power generation at this location. Furthermore, the agreement between the turbulence-based and speed profile estimates of stress in Fig. 20 provides positive support for remotely estimating turbulence quantities in mid-water column from high sampling rate ADCP data: in particular, the turbulent kinetic energy

$$q^2/2 = \left[\langle u'^2\rangle + \langle v'^2\rangle + \langle w'^2\rangle\right]/2\ . \qquad (14)$$

Since the xz measurement plane is aligned with the isobaths, and the ADCP registered near 0° roll (Fig. 11), the u'^2 and w'^2 contributions can be determined from the spectra of the u and w time series. However, because of the ca. -8° pitch, the beam 3 and beam 4 range bins are at different heights (and depths). A choice must be made between depth and height for a common level at to determine v from $V3$ and $V4$. Because the flow is aligned with the bottom contours at the ADCP site (Figs. 10a and 10b), and the bed slope transverse to the flow is more or less constant on O(10 m) horizontal scales (i.e. the scale of the beam separation), it is reasonable to assume that the thickness of the lower boundary layer would also be uniform on this scale. Our finding that the near-bed transverse Reynolds stress is zero on average (Fig. 20) is consistent with this assumption. Thus, the logical choice here for the common level between beams 3 and 4, within the lower boundary layer (i.e. within and immediately above the constant stress layer), is height above bottom. It follows that the three terms contributing to q^2 can be determined from the velocity components in instrument coordinates.

Estimates of q^2 were obtained from the integrals of the instrument coordinate velocity component spectra after subtracting the observed noise floor (0.0106 m^2/s^2/Hz for u' and v', and 0.0014 m^2/s^2/Hz for w'), and ensemble averaging in 0.2 m/s (depth-averaged) speed bins. Note that the 0.0106 m^2/s^2/Hz noise floor observed in S_{uu} and S_{vv} corresponds to an equivalent velocity accuracy of 0.099 m/s, very close to the manufacturer's value of 0.096 m/s (see §III-B). The resulting RMS turbulence intensity (i.e. q) is plotted in Fig. 24 for heights less than 10 m, versus depth-averaged mean speed U. For speeds above 0.2 m/s, the ratio q/U at a given height is roughly constant, with values lying between 0.1 and 0.2, typical of the range of design values in the wind turbine literature. Here however the values are higher for ebb than flood, as expected from the results in §III-B, C, D and Fig. 23, and tend to decrease with height, indicating higher intensity turbulence nearer the bed, also as expected from turbulent boundary layer physics. (This behaviour is absent at and above 1.5 m/s, and is reversed at speeds below 0.5 m/s. The former is likely due to the smaller number of realizations at high mean speeds. The latter indicates that, at low speeds, turbulence generated within the bottom boundary layer locally is less intense than turbulence in mid-water column, presumably generated upstream.)

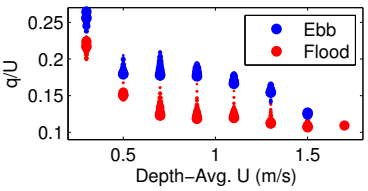

Fig. 24. ADCP: RMS turbulence intensity q, normalized by the depth-averaged mean speed U, vs. U, for heights between 2.1 and 10.1 m. Symbol size increases with height.

V. Conclusion

The following conclusions are drawn:

1) The MAVS results – i.e. a well-defined inertial subrange and agreement with $\sigma_w = 1.2u_*$ – indicate that this sensor represents a useful alternative for turbulence measurements, particularly in clear water conditions.

2) Broadband ADCP noise levels can be reliably estimated from spectra ensemble-averaged into rank-ordered speed bins.

3) When the constant stress layer was sufficiently thick – i.e. during ebb tide – the ADCP alongbeam velocity spectra exhibit a well-defined inertial subrange. In addition, the noise-corrected variances determined from these spectra are entirely consistent with the anisotropy relations for turbulent velocity component standard deviations in the constant stress layer from atmospheric boundary layer measurements: $\sigma_u = 2u_*$, $\sigma_v = 1.4u_*$, $\sigma_w = 1.2u_*$ [1] [13].

4) Estimates of the stream-wise Reynolds stress from ADCP beam coordinate velocities within the constant stress layer – via the variance method – are equal on average to the bed shear stress determined via the Law-of-the-Wall.

5) Estimates of the cross-stream Reynolds stress from ADCP bins within the constant stress layer are near zero on average, consistent with a first-order dynamic balance for channelized along-isobath unstratified flow with near zero cross-stream pressure gradient.

6) Unlike the findings of Stacey *et al* [5], vertical profiles of the streamwise Reynolds stress from the ADCP are markedly different from the linear profile expected for flow in straight, narrow open channels [17]. The higher Reynolds number, and more irregular bathymetry and lateral boundaries in Grand Passage compared to Three Mile Slough are likely causes [5].

7) Pronounced differences are observed between flood and ebb tide – in the thicknesses of the logarithmic and constant stress layers, in the ratio of RMS turbulence intensity to mean speed, and in the bottom drag coefficient – likely related to and mediated by differences in upstream bathymetry.

8) For depth-averaged mean speeds of ca. 0. 5 m/s and higher, and heights up to 10 m, the ratio of RMS turbulence intensity to mean speed lies in the range 0.1 to 0.2, though it is systematically lower during flood than ebb, and decreases with height above bottom. At 10 m (i.e. the nominal "hub height" here), this ratio falls between 0.16 and 0.18 during ebb, and between roughly half these values during flood.

Acknowledgment

We thank the skipper and crew of the *MV Expectations XL*. Rolf Lueck, Len Zedel, Peter Taylor, and Richard Dewey each provided valuable input. This work was funded by the Offshore Renewable Energy Association and by the Natural Sciences and Engineering Research Council of Canada.

References

[1] M. R. Raupach, R. A. Antonia, and S. Rajagopalan, "Rough wall turbulent boundary layers," *Appl. Mech. Rev.*, vol. 44, pp. 1–25, 1991.

[2] A. J. Plueddemann, "Observation of the upper ocean using a multi-beam Doppler sonar," Ph.D. thesis, Scripps Institution of Oceanography, La Jolla, 1987.

[3] A. Lohrmann, B. Hackett, and L. P. Roed, "High resolution measurements of turbulence, velocity and stress using a pulse-to-pulse coherent sonar," *J. Atmos. Oceanic Tech.*, vol. 7, pp. 19–37, 1990.

[4] A. E. Gargett, "Observing turbulence with a modified acoustic Doppler profiler," *J. Atmos. Ocean. Tech.*, vol. 11, pp. 1592–1610, 1994.

[5] M. T. Stacey, S. G. Monismith, and J. R. Burau, "Measurements of Reynolds stress profiles in unstratifiedtidal flow," *J. Geophys. Res.*, vol. 104, no. C5, pp. 10,933–10,949, 1999.

[6] Y. Lu, R. G. Lueck, and D. Huangf, "Turbulence characteristics in a tidal channel," *J. Phys. Oceanogr.*, vol. 30, pp. 855–867, 2000.

[7] T. P. Rippeth, J. H. Simpson, E. Williams, and M. E. Inall, "Measurements of the rates of production and dissipation of turbulent kinetic energy in an energetic tidal flow: Red Wharf Bay revisited," *J. Phys. Oceanogr.*, vol. 33, pp. 1889–1901, 2003.

[8] Y. Lu and R. G. Lueck, "Using a broadband ADCP in a tidal channel. Part II: Turbulence," *J. Atmos. Ocean. Technol.*, vol. 16, pp. 1568–1579, 1999.

[9] E. Williams and J. H. Simpson, "Uncertainties in estimates of Reynolds stress and TKE production rate using the ADCP variance method," *J. Atmos. Ocean. Technol.*, vol. 21, pp. 347–357, 2004.

[10] B. Vermeulen, A. J. F. Hoitink, and M. G. Sassi, "Coupled ADCPs can yield complete Reynolds stress tensor profiles in geophysical surface flows," *Geophys. Res. Lett.*, vol. 38, 2011, l06406, doi:10.1029/2011GL046684.

[11] J. Thomson, B. Polagye, V. Durgesh, and M. C. Richmond, "Measurements of turbulence at two tidal energy sites in Puget Sound, WA," *IEEE J. Oceanic Eng.*, 2012, doi 10.1109/JOE.2012.2191656.

[12] B. Gunawan and V. S. Neary, "ORNL ADCP post-processing guide and Matlab algoritms for MHK site flow and turbulence analysis," Oak Ridge National Laboratory, Tech. Rep. ORNL/TM-2011/404, 2011.

[13] J. C. Wyngaard, *Turbulence in the Atmosphere*. Cambridge, U.K.: Cambridge University Press, 2010.

[14] A. J. Williams 3rd and F. T. Thwaites, "Earth coordinate 3-d currents from a modular acoustic velocity sensor," *Oceans 98*, vol. IEEE Catalog Number, no. 98CH36259, pp. 244–247, 1998.

[15] A. J. Williams 3rd, G. Ryan, and F. T. Thwaites, "Oversampling MAVS for reduction of vortex-shedding velocity-sensing noise," *Oceans 2012*, ISBN 978-1-4673-0829-8.

[16] M. R. Raupach, "Conditional statistics of Reynolds stress in rough-wall and smooth-wall turbulent boundary layers," *J. Fluid Mech.*, vol. 108, pp. 363–382, 1981.

[17] I. Nezu and H. Nakagawa, *Turbulence in Open Channel Flows*. A. A. Balkema, Brookfield, Vt., 1993.

[18] K. R. Sreenivasan, "On the universality of the Kolmogorov constant," *Phys. Fluids*, vol. 7, no. 11, pp. 2,778–2,784, 1995.